

Chandra Observations of Candidate “True” Seyfert 2 Nuclei

Himel Ghosh, Richard W. Pogge, Smita Mathur, Paul Martini

*Department of Astronomy, The Ohio State University
140 W 18th Ave, Columbus, OH 43210*

ghosh,pogge,smita,martini@astronomy.ohio-state.edu

and

Joseph C. Shields

*Department of Physics & Astronomy, Ohio University
Clippinger Lab 251B, Athens, OH 45701*

shields@phy.ohiou.edu

ABSTRACT

The Unification Model for active galactic nuclei posits that Seyfert 2s are intrinsically like Seyfert 1s, but that their broad-line regions (BLRs) are hidden from our view. A Seyfert 2 nucleus that truly lacked a BLR, instead of simply having it hidden, would be a so-called “true” Seyfert 2. No object has as yet been conclusively proven to be one. We present a detailed analysis of four of the best “true” Seyfert 2 candidates discovered to date: IC 3639, NGC 3982, NGC 5283, and NGC 5427. None of the four has a broad H α emission line, either in direct or polarized light. All four have rich, high-excitation spectra, blue continua, and *Hubble Space Telescope* (*HST*) images showing them to be unresolved sources with no host-galaxy obscuration. To check for possible obscuration on scales smaller than that resolvable by *HST*, we obtained X-ray observations using the *Chandra X-ray Observatory*. All four objects show evidence of obscuration and therefore could have hidden BLRs. The picture that emerges is of moderate to high, but not necessarily Compton-thick, obscuration of the nucleus, with extra-nuclear soft emission extended on the hundreds-of-parsecs scale that may originate in the narrow-line region. Since the extended soft emission compensates, in part, for the nuclear soft emission lost to absorption, both absorption and luminosity are likely to be severely underestimated unless the X-ray spectrum is of sufficient quality to distinguish the two components. This is of special concern where the source is too faint to produce a large number of counts, or where the source is too far away to resolve the extended soft X-ray emitting region.

Subject headings: galaxies: active — galaxies: nuclei — galaxies: Seyfert — X-rays: galaxies

1. Introduction

Seyfert Galaxies are relatively low-luminosity Active Galactic Nuclei (AGNs) that are traditionally divided into two types, 1 and 2, following an empirical optical spectroscopic classification scheme proposed over 30 years ago by Khachikian & Weedman (1974). Seyfert 1s are characterized by strong, broad (widths of several thousand km s^{-1}) permitted emission lines of Hydrogen, Helium, and Fe II and narrow (typical widths of $500 - 1000 \text{ km s}^{-1}$) forbidden lines such as [O III], [N II], and [S II]. Seyfert 2s have only narrow permitted and forbidden lines of comparable width and are characterized by a very high [O III] $\lambda 5007/\text{H}\beta$ line ratio. Both classes also often exhibit a blue featureless continuum, often manifested as an “ultraviolet excess,” though this is not a necessary criterion.

The leading explanation for the spectral differences between the two classes of Seyferts is the Unification Model originally motivated by observations of polarized broad emission lines in a number of Seyfert 2 galaxies (Antonucci 1993, and references therein). Unification posits that all Seyfert galaxies have the same underlying structure: a central continuum source arising from an accretion disk around a central supermassive black hole, a dense broad-line region (BLR) comprised of high-velocity gas located on light-day scales, and a low-density narrow-line region (NLR) on parsec scales. The BLR is nestled inside a torus of dusty obscuring material surrounding the nucleus, and whether we see a Type 1 or 2 spectrum depends on the orientation of this torus with respect to our line of sight (see Peterson 1997, Fig 7.1). In Seyfert 1s we are looking down the opening of the torus and see the BLR and central continuum source, while in Seyfert 2s the torus blocks the central regions from view and we only see the narrow-line spectrum of the NLR. In some Seyfert 2s a circumnuclear cloud of gas in a favorable location outside the torus opening acts as a polarizing “mirror” that affords an oblique view down the unobscured axis of the torus, and we see the BLR and underlying continuum in polarized light. A large fraction of the Seyfert 2s observed with spectropolarimetry to date have polarized broad lines (Moran et al. 2000; Tran 2001; Lumsden et al. 2001; Lumsden, Alexander, & Hough 2004).

Additional support for the Unification scenario comes from X-ray studies that have demonstrated that many Seyfert 2s are highly absorbed at soft X-rays by very large column densities ($\log N_H > 23$, e.g., Mulchaey et al. 1994; Maiolino et al. 1998; Guainazzi et al. 2001). Indeed, this idea has become so compelling that many obscured AGNs, especially those that are X-ray bright but have no or only very weak optical counterparts, are called “Type 2 AGN”, often regardless of whether or not their optical spectra satisfy the original Khachikian & Weedman criteria.

While there is little doubt that a large fraction of Seyfert 2s are indeed obscured Seyfert 1s, there is still no good answer to the question of whether or not there exists a subset of spectroscopically-classified Seyfert 2s that intrinsically lack a BLR. Such BLR-free Seyfert 2s have variously been called “true Seyfert 2s” (e.g., Boisson & Durret 1986) or “pure Seyfert 2s” (e.g., Heckman et al. 1995) to distinguish them from the Seyfert 2s that are hidden Seyfert 1s in the Unification picture. We shall adopt the term “true Seyfert 2s” in this investigation. Our motivation

in taking up this question is not to attempt to disprove the Unification picture, but rather to try to find the interesting exceptions to it. Identifying and studying objects that lie at the extremes of the parameter space for the accretion process are critical for informing us about the important physical details of that process.

Why might there be no BLR in some AGN? Recent observations and theoretical work have suggested that the gas responsible for the BLR is related, at least in part, to the accretion process (e.g., a high-velocity outflow from the disk, Murray & Chiang 1998). One possibility is that as an AGN becomes active, there is a brief period where conditions conducive to formation of a BLR have not yet been established. Similarly, when an AGN turns off there might come a time during the shutdown when the BLR can no longer be sustained. The high densities and small scale (few light days) of the BLR means it responds very rapidly to changes in the ionizing continuum, whereas the low-density, extended scale (10s to 100s of parsecs) of the NLR leads to a slower response by many orders of magnitude: the BLR sees the central continuum as it was days ago, whereas the NLR would see it as it was decades to centuries ago. Historically, at least a few Seyfert 1s have been observed during extremely low continuum states in which the broad components of the Balmer lines have practically vanished for a brief time, e.g., NGC 4151 (Penston & Perez 1984), NGC 1566 (Alloin et al. 1985), and Mrk 1018 (Cohen et al. 1986).

Another possibility is that there are natural limits to the existence of a BLR. Nicastro (2000, also Nicastro et al. 2003) has proposed a scenario in which the broad lines arise in a disk wind that requires a minimum accretion rate, and the BLR naturally vanishes in low-luminosity objects that fall below the minimum accretion-rate threshold. Laor (2003) has likewise proposed that the BLR may vanish in low-luminosity AGNs, based on extrapolations of empirical scaling relations for luminosity, BLR size scale, and line widths that have been discovered in studies of AGN spectral variability (see Peterson et al. 2004).

Whatever the root cause, at first sight a true Seyfert 2 would be virtually indistinguishable from a Seyfert 2 with a hidden BLR and thus hard to identify without a fair amount of supplementary data. If the picture that they are related to low accretion-rate objects is correct, they would be expected to be relatively rare and primarily identifiable only among nearby AGN. Thus far, really convincing true Seyfert 2s have proven elusive. This paper presents an attempt to confirm true Seyfert 2 candidates from the local, spectroscopically-identified Seyfert 2 population by using X-ray measurements to determine if an obscuring medium is present.

This paper is organized as follows: §2 describes how the *Chandra* targets were selected; §3 describes the observations and analysis of the data, with individual targets discussed in §3.1–3.4; the results are discussed in §4; a summary is presented in §5.

2. Sample selection

Selection of candidate true Seyfert 2 nuclei proceeds by a process of elimination. We started with a sample of local ($v < 3000 \text{ km s}^{-1}$) AGN taken from galaxies in the CfA Redshift sample (Huchra & Burg 1992; Osterbrock & Martel 1993) and the Revised Shapley-Ames (RSA) Catalog (Sandage & Tammann 1987) as described by Regan & Mulchaey (1999). Previous “structure mapping” image processing of a subset of these galaxies (Pogge & Martini 2002) showed that a number of the Seyfert 2s have bright, unresolved star-like nuclei with no apparent evidence of host-galaxy scale absorption (e.g., as seen in some Seyfert 2s by Malkan, Gorjian, & Tam 1998). We start with these to eliminate those nuclei that are obscured by kiloparsec-scale dust lanes in the host galaxies. Of the remaining “stellar” nuclei Seyfert 2s, we eliminate all of those with previous spectropolarimetric detections of broad $\text{H}\beta$ or $\text{H}\alpha$ emission lines, and thus archetypal hidden Seyfert 1s.

The final selection employed long-slit optical spectrophotometry of the nuclei acquired with the *STIS* instrument on *HST* as part of a separate, on-going study of Seyfert 2s with unobscured, stellar nuclei (Pogge et al. 2006). Of the nine Seyfert 2s without broad $\text{H}\alpha$ emission lines seen in direct or polarized light, four have red continua and narrow Balmer emission-line ratios consistent with significant line-of-sight extinction, and thus were rejected from further consideration. This left us with a final sample of five Seyfert 2s — IC 3639, NGC 3982, NGC 5283, NGC 5427, NGC 5347 — all of which have blue featureless continua; rich, high-excitation spectra with highly-ionized species like $[\text{Fe X}]$, $[\text{Fe VII}]$ and $[\text{Ne V}]$; and most of the emission arising from an unresolved region within $\sim 20 \text{ pc}$ of the active nucleus.

Our procedure was therefore to identify true Seyfert 2 candidates by eliminating Seyfert 2s with substantial host galaxy obscuration (using morphological data), hidden BLRs (using spectropolarimetry), and unresolved obscuration on small scales (using the presence of blue nuclear continua and strong, high-excitation lines). There were no archival X-ray data available to use at the time that would permit an assessment of the X-ray absorption arising on much smaller scales, so we applied for and were granted time during *Chandra* AO5 to acquire observations of 4 of these: IC 3639, NGC 3982, NGC 5283, NGC 5427. Observations of NGC 5347 were awarded to another program (Levenson et al. 2006).

3. Observations and Data Analysis

The four targets were observed between November 2003 and March 2004 for 10 ks each, resulting in about 9 ks of usable exposure time on each object. Details of the observations are given in Table 1. Each observation used the S3 chip in ACIS in 1/8 sub-array mode. All of the targets were detected.

The data were processed using version 3.1 of the Chandra Interactive Analysis of Observations

(CIAO) package. Level 2 event lists were re-processed with observation-specific bad pixel files. The event lists were then converted to FITS images and the CIAO wavelet source detection tool *wavdetect* was run to determine source positions. For each observation, source counts were extracted from a circular aperture centered on the *wavdetect* source position and with a radius of 4.67 pixels (or $2.3''$, 1.3 times the on-axis 95% encircled-energy radius at 1.5 keV on ACIS-S). This aperture ensured that virtually all photons from a point source would be included. Background counts were taken from an annulus with an inner radius of twice, and an outer radius of five times, the source circle radius, after excising any point sources that fell within the annulus. While it is true that diffuse extended emission from the host galaxy, if any, would have been included in the background, it does not affect our analysis since we are concerned with the nucleus and the much brighter circumnuclear emission. Counts were extracted in the 0.3 – 8.0 keV (Broad), 2.5 – 8.0 keV (Hard) and 0.3 – 2.5 keV (Soft) bands. A hardness ratio (HR) was defined as $HR = (H - S)/(H + S)$, where H and S are the counts in the hard and soft bands, respectively. Source counts and hardness ratios are given in Table 2. Further processing on individual objects is described in the sections that follow. In general, for the two objects where the data are of sufficient quality for spectral fitting, unbinned pulse invariant (PI) spectra in the energy range 0.3 – 8.0 keV were created as described by the applicable CIAO “Science Thread” at the website¹ of the Chandra X-Ray Center (CXC). Spectral fitting was performed using the CIAO tool *Sherpa*. Spectral fits are summarized in Table 3.

Though the soft emission in the spectra we fit is likely dominated by emission lines, our spectra have too low signal-to-noise ratio to identify lines or blends of lines. The best that can be done is to fit the upper envelope of the lines, and even this is not very well constrained. Therefore, for the sake of simplicity and ease of fitting we use a thermal bremsstrahlung model for the soft component, rather than a more physically plausible but multi-parameter model like MEKAL.

3.1. IC 3639

The nucleus of IC 3639 is clearly detected, with 283 counts. As can be seen from Fig. 1, there is an extended component to the emission and this extended emission is soft.

The spectrum was extracted using the circular aperture described above. Our extracted nuclear spectrum includes the extended component because there are not enough counts to fit separate spectra to the nuclear and extended components. Before fitting, the source spectrum PI channels were binned so that each bin had at least 20 counts. The low number of counts did not justify the extra parameters that would be introduced by using models that have different absorbers for the nuclear and extended emission, and therefore we assumed a single absorber for both components. Since the extended soft emission is included, it is not surprising that a simple, absorbed power-law

¹<http://cxc.harvard.edu/ciao/threads/pieces/>

model (`powlaw1d` and `xswabs` in *Sherpa*) does not fit the spectrum well ($\chi^2_\nu = 3$)². Adding a thermal bremsstrahlung component (`xsbremss`) with $kT = 0.11 \pm 0.03$ keV provides an acceptable fit ($\chi^2_\nu = 0.9$). The resulting best-fit values for the power-law index³ and column density are $\Gamma = 2.61 \pm 0.60$ and $N_H = (8.9 \pm 2.4) \times 10^{21} \text{ cm}^{-2}$, respectively. The spectrum along with the best-fit model and residuals are shown in Fig. 2. The spectrum suggests that we are probably detecting an AGN with intrinsic power-law emission and moderate to heavy absorption. The absorbing column density is not well constrained due to the presence of the extended, soft component.

If we use bins of constant width, rather than bins with a minimum number of counts, then there is evidence for an emission line at ~ 6.4 keV, albeit at low signal-to-noise level. We therefore tried a fit with a reflection component. A thermal component with $kT = 0.20 \pm 0.02$ keV is still required. The best-fit position of the line is at 6.38 ± 0.07 keV. The equivalent width of the line has a best-fit value of 500 eV but is unconstrained by the fit. Similarly, the reflection parameter, which describes how much of the observed emission can be attributed to reflection, is unconstrained but has a best-fit value of 0.6. The right panels of Fig. 2 show the fit, consisting of thermal bremsstrahlung and a reflected power law, both absorbed, plus an unresolved line.

The model flux in the bremsstrahlung component (0.5–2 keV, but effectively 0.5 – 10 keV, since there is almost no flux between 2 and 10 keV) is $7.1 \times 10^{-12} \text{ erg cm}^{-2} \text{ s}^{-1}$ after correcting for absorption ($6.3 \times 10^{-14} \text{ erg cm}^{-2} \text{ s}^{-1}$ observed), which implies a luminosity $L_{0.5-2 \text{ keV}} = 1.9 \times 10^{42} \text{ erg s}^{-1}$. The absorption-corrected AGN luminosities according to the model are $L_{2-10 \text{ keV}} = 1.7 \times 10^{40} \text{ erg s}^{-1}$ and $L_{0.5-10 \text{ keV}} = 5.3 \times 10^{40} \text{ erg s}^{-1}$, or about 3% of the luminosity of the extended component.

3.2. NGC 3982

The nucleus of NGC 3982 was detected with 73 counts. Figure 3 shows the *Chandra* image and a hardness ratio map. Most of the emission is in the soft band. The source does not appear extended. The small number of counts precludes any detailed spectral fitting, but we attempted several two-parameter fits (one interesting parameter and its normalization) with the column density fixed at the Galactic value towards this target ($1.23 \times 10^{20} \text{ cm}^{-2}$). After binning the PI channels so that there were at least 15 counts in each bin, a power-law model gives a best-fit value of $\Gamma = 3.7 \pm 0.9$. However, a single power law does not provide a good fit ($\chi^2_\nu \sim 3.3$) as can be seen in the left panels of Fig. 4.

Considering the possibility that the entire emission seen could be from circumnuclear gas, such as is present in IC 3639, the spectrum was also fit with a thermal bremsstrahlung model and a model with both power-law and thermal components. The former gives a best-fit value of $kT = 0.54 \pm 0.15$

² χ^2_ν is the χ^2 per degree of freedom.

³This is a photon index. The number of photons as a function of energy is assumed to be given by $N(E) \propto E^{-\Gamma}$.

keV, with $\chi^2_\nu = 3.3$. The latter fit was performed by first fitting a bremsstrahlung model to the data points below 2 keV, then freezing the model and fitting a combined thermal plus power law model to data in the full energy range, 0.3–8.0 keV. This produces a nominally better fit, with $\chi^2_\nu = 1.6$, but fails to constrain any of the fit parameters. The best-fit values are $kT = 0.48$ keV and $\Gamma = -1.6$. The above fit was also re-done with absorption as a free parameter, but keeping the power law index and temperature of the thermal emission fixed. For $\Gamma = 2$, the fit returns $N_H = (2.2 \pm 0.9) \times 10^{21} \text{ cm}^{-2}$ and $kT = 0.13$ keV. The best-fit values were obtained by varying the (fixed) values of Γ and kT and re-fitting, giving $N_H = (2.3 \pm 0.9) \times 10^{21} \text{ cm}^{-2}$, $\Gamma = 1.0$ and $kT = 0.13$ keV. This fit is shown in the right panels of Fig. 4.

3.3. NGC 5283

NGC 5283 is the brightest of the four targets, with 454 counts. The *Chandra* image (Fig. 5) clearly shows extended emission to the northwest and southeast of the central source. This object is different from the other three in that its hardness ratio is positive, i.e. there is more emission in the hard band. It is similar to IC 3639 in that there is a central source surrounded by extended soft emission — in this case the point source is hard, and bright enough to dominate the total emission. Spectral fits were performed with PI channels binned so that each bin had at least 20 counts. The spectrum (Fig. 6) shows a power law at high energies (best-fit $\Gamma = 1.46 \pm 0.33$), but with a turn-over at ~ 4 keV, indicating strong absorption (best-fit $N_H = [7.5 \pm 3.0] \times 10^{22} \text{ cm}^{-2}$). There is a significant “soft excess” which can be fit by a thermal bremsstrahlung model with best-fit $kT = 0.79 \pm 0.31$ keV.

Most of the soft emission is from the extended feature seen in Fig. 5 and we therefore extracted spectra of this emission and the nuclear emission separately. The top panel of Fig. 7 shows a spectrum of just the diffuse emission. This was extracted from a 12-pixel \times 8-pixel rectangle which encompassed the entire extended emission, but with a 3 \times 3 island centered on the brightest pixel masked out. The bottom panel shows a spectrum of just the central pixel. Of note about this object is that *no* fit was possible if the thermal component and the power law were assumed to be absorbed by the same gas. The only acceptable fits required a much lower column density for the material absorbing the thermal emission than for the material absorbing the power law emission. Confidence regions for the spectral model parameters are shown in Fig. 8.

The best-fit model gives absorption-corrected nuclear luminosities of $L_{2-10 \text{ keV}} = 6.3 \times 10^{41} \text{ erg s}^{-1}$ and $L_{0.5-10 \text{ keV}} = 7.1 \times 10^{41} \text{ erg s}^{-1}$, and the extended emission has $L_{0.5-2 \text{ keV}} = 9.9 \times 10^{39} \text{ erg s}^{-1}$. The AGN is brighter by a factor of ~ 65 .

3.4. NGC 5427

Figure 9 shows the *Chandra* image of the nucleus NGC 5427. Only 35 counts were detected, almost all (33) in the soft band, giving it a hardness ratio of -0.9 . If this source is similar to the others, then the faintness and lack of hard emission suggest we are detecting only the circumnuclear soft emission and the central point source is heavily absorbed. Figure 10 shows the spectrum, which has been binned so that there are at least 5 counts in each bin. As with the other targets, a thermal bremsstrahlung model ($kT = 0.7$ keV) with Galactic absorption was “fit” to the data. However, there are not sufficient data to discriminate among models. The data are equally consistent with a model where the source is assumed to consist of absorbed thermal bremsstrahlung and a power law.

4. Discussion

Although targeted as candidate true Seyfert 2s, or AGNs without BLRs, the four objects studied here — IC 3639, NGC 3982, NGC 5283, and NGC 5427 — all show evidence of obscuration when observed in X-rays. They are therefore not good “true” Seyfert 2 candidates, though of course the presence of obscuration does not imply the existence of a BLR behind the obscuration. The picture that emerges is of moderate to high, but not necessarily Compton-thick, obscuration of the nucleus, $N_H \sim \text{few} \times 10^{21} - 10^{22} \text{ cm}^{-2}$, and extended soft emission on hundreds-of-parsecs scales that may possibly originate in the NLR.

The spectrum of IC 3639 shows moderate absorbing column densities and possibly a reflection component, with an Fe $K\alpha$ line detected with low significance. The spectrum of NGC 5283 clearly shows a power law which is strongly absorbed below ~ 4 keV. The spectra of both objects require a separate component to fit the soft emission. This component is probably a result of the blending of multiple emission lines from a photoionized gas (Bianchi, Guainazzi & Chiaberge 2006); however, the CCD spectra analyzed here are not of high enough quality to constrain a multi-parameter model like APEC or MEKAL, and the soft emission was equally well fit by a thermal bremsstrahlung model and a pure blackbody spectrum. In either case the characteristic temperature turns out to be a few tenths of a keV. That the soft and hard components originate in physically distinct regions is suggested by the hardness ratio maps themselves (Figs. 1 and 5), which show harder emission surrounded by extended softer emission. In the case of NGC 5283, which has sufficient counts, this was shown more definitively by fitting the spectra of the nucleus and the surrounding emission separately. The harder, power law component clearly is stronger closer to the nucleus, while the extended emission is dominated by the soft component. The extended, soft component also has a lower obscuring column than the nuclear emission.

The two fainter objects, NGC 3982 and NGC 5427, while too faint to make spectral fitting possible, appear to be consistent with the above picture. The observed emission is soft: NGC 3982 has a hardness ratio of -0.7 and NGC 5427 does not even have a statistically significant detection

in the hard band. The faintness is not due to distance — these two objects are in fact nearer than the two brighter ones. All four nuclei observed here have comparable [O III] luminosities (Whittle 1992; Nelson & Whittle 1995) and thus are expected to have comparable L_X (Heckman et al. 2005). These two fainter objects may therefore be even more heavily obscured and we are primarily detecting soft X-ray emission from hot, extra-nuclear gas. Is this gas itself responsible for part of the absorption of the nucleus? While not clear in IC 3639, in NGC 5283 the gas spectrum is consistent with only Galactic absorption, whereas the nuclear spectrum requires an additional column density of $N_H \sim 10^{22} \text{ cm}^{-2}$. In the Laor (2003) model, the innermost part of an NLR would become a warm absorber, with the effect getting stronger for lower-luminosity AGN.

The gas emitting soft X-rays has the right physical scale (few hundred parsecs) to be the gas that constitutes the NLR, and Bianchi, Guainazzi & Chiaberge (2006) find that in their sample of Seyfert 2s the morphology of the X-ray gas matches that of the NLR as determined by [O III] $\lambda 5007$ imaging. Figures 11 and 12 show structure maps (Pogge & Martini 2002) made from wide-band (F606W) *HST* images of IC 3639 and NGC 5283, respectively, with X-ray contours overlaid. The NLRs are identifiable as bright regions near the centers of the images, and the contours show that the X-ray emission is extended in the same orientation as the NLRs. NGC 3982 and NGC 5427, which do not show prominent, extended X-ray emission, also do not show extended NLR emission in structure maps (Pogge & Martini 2002). If the soft X-ray-emitting gas is really the NLR, then the source of ionizing radiation is presumably the central engine, and not a starburst. The soft X-ray (0.5–2 keV) luminosity of IC 3639 inferred from the spectral fit, $L_{0.5-2\text{keV}} \sim 10^{42} \text{ erg s}^{-1}$, would imply a star formation rate (SFR) of $\sim 100 M_\odot \text{ yr}^{-1}$ (Hornschemeier et al. 2005). This is an order of magnitude higher than the known SFR of IC 3639 derived from its infrared luminosity ($\sim 9 M_\odot \text{ yr}^{-1}$, Dopita et al. 2002) and favors the central engine as the ionizing source. For NGC 5283, $L_{0.5-2\text{keV}} \sim 10^{40} \text{ erg s}^{-1}$, requiring an SFR of only a few $M_\odot \text{ yr}^{-1}$, which is consistent with what is known based on its infrared luminosity (Kennicutt 1998; Pérez García & Rodríguez Espinosa 2001), and star formation cannot be ruled out, but the AGN luminosity of $\sim 10^{42} \text{ erg s}^{-1}$ could explain the ionized gas without star formation. For IC 3639, the [O III] to soft X-ray flux ratio $F_{\lambda 5007}/F_{0.5-2\text{keV}} \approx 5 - 6$, while the ratio for NGC 5283 is $F_{\lambda 5007}/F_{0.5-2\text{keV}} \approx 0.6$, a range similar to that seen in the Bianchi, Guainazzi & Chiaberge (2006) sample. Higher quality spectra of similar, absorbed Seyferts indicate that the soft X-ray emission consists of blended emission lines from a photoionized gas (e.g. Bianchi, Guainazzi & Chiaberge 2006; Levenson et al. 2006). Thus, morphology, energetics, and spectra all suggest that the NLR is the source of the soft X-ray emission seen in at least some Seyfert 2s.

Though obscuration prevents any deductions about the presence or absence of BLRs in these objects, we apply the Laor (2003) model to our objects to determine if the unobscured luminosities are still consistent with his model. This model predicts a minimum bolometric luminosity (as a function of black hole mass) needed to sustain a BLR. We obtained published stellar velocity dispersions from Whittle (1992), Nelson & Whittle (1995) and Garcia-Rissmann et al. (2005), [O III] fluxes from Whittle (1992) and Nelson & Whittle (1995), and used the conversion from Heckman

et al. (2004) to change [O III] luminosities to bolometric luminosities. A comparison with Fig. 1 of Laor (2003) shows that all four of our nuclei have luminosities ($\log(L_{\text{bol}}/\text{erg s}^{-1}) \sim 44, 43, 44, 43$ for IC 3639, NGC 3982, NGC 5283, NGC 5427, respectively) well above the minimum needed to have a BLR. In the case of NGC 5283, the absorption-corrected 2–10 keV luminosity that we obtain from the X-ray spectral fit would be by itself greater than the minimum required. Therefore none of the four is a true Seyfert 2 according to the Laor (2003) model.

Observations of these four objects show that it can be misleading if we depend only on the hardness ratio to estimate absorption for sources with a small number of counts. For example, NGC 3982 has an $\text{HR} = -0.7$, which is the HR expected with ACIS-S for a canonical unabsorbed AGN spectrum. What is being measured, however, is the HR of the NLR, with some hard-band contamination from the partially-obscured nuclear source. This is of special concern in cases where very few counts are detected and the hardness ratio is the only quantity that can be determined with any certainty. If any extended soft emission is not taken into account, the true absorption will be underestimated, and the calculated X-ray luminosity will be too low. Even when spectral fitting is possible, if the spectrum is not of sufficient quality to distinguish the two components, an absorbed AGN may mimic an unobscured AGN of lower luminosity. Several, or all, of the apparently unobscured Seyfert 2s that have been discovered so far (e.g. Pappa et al. 2001; Panessa & Bassani 2002; Barcons, Carrera, & Ceballos 2003; Gezari et al. 2003; Georgantopoulos & Zezas 2003) are probably examples of exactly this kind of mistaken identity. None of these objects has observations with the angular resolution and high signal-to-noise spectrum necessary to rule out the scenario we propose for our sample. Faint AGN at moderate redshift, such as those being found in the deep X-ray surveys, are particularly susceptible to such misclassification. These sources are extremely important because some intrinsically high-luminosity AGN may be masquerading as apparently low-luminosity Seyfert 1s. These obscured AGN are exactly the sources invoked to explain the spectrum of the cosmic X-ray background (Brandt & Hasinger 2005). Also affected is the estimation of the AGN luminosity function.

5. Summary

We identified four Seyfert 2 nuclei — IC 3639, NGC 3982, NGC 5283, and NGC 5427 — that appeared to be unobscured based on optical and UV *HST* data, yet did not have broad lines in either direct or polarized light. The apparent lack of obscuration made these good “true” Seyfert 2 candidates, that is AGNs that genuinely lack a BLR. Since there still could be obscuration on scales smaller than that resolvable by *HST*, we obtained X-ray observations, as X-rays are presumed to originate close to the central engine and therefore may “see” absorbing material that exists on very small scales, yet hard X-rays have high enough energy that they are expected to penetrate the absorbing material. A lack of X-ray absorption would point to the lack of an obscured BLR. However, all four nuclei show signs of obscuration when observed in X-rays. Spectral fits were possible for IC 3639 and NGC 5283, and imaging and spectra indicate an unresolved, moderately

absorbed ($N_H \sim 10^{21-22} \text{ cm}^{-2}$) nucleus with a hard spectrum surrounded by extended soft emission. Data for the other two objects are consistent with this picture although their X-ray spectra are of much lower signal-to-noise ratio. A comparison of the X-ray and optical images suggests that the soft X-ray emission arises in the narrow-line region. Finally, we note that in cases where the extended emission region is not resolved, and the spectrum obtained does not have a high enough signal-to-noise ratio, it may not be possible to distinguish the nuclear and non-nuclear components. In such cases an intrinsically bright but absorbed AGN may be mistaken for an intrinsically faint, unabsorbed AGN.

Support for this work was provided by the National Aeronautics and Space Administration through Chandra Award Number GO4-5114A issued by the Chandra X-ray Observatory Center, which is operated by the Smithsonian Astrophysical Observatory for and on behalf of the National Aeronautics Space Administration under contract NAS8-03060.

Facilities: CXO (ACIS), HST (WFPC2)

Data Sets: 4844, 4845, 4846, 4847

REFERENCES

- Alloin, D., Pelat, D., Phillips, M., & Whittle, M. 1985, *ApJ*, 288, 205
- Antonucci, R. 1993, *ARA&A*, 31, 473
- Barcons, X., Carrera, F. J., & Ceballos, M. T. 2003, *MNRAS*, 339, 757
- Bianchi, S., Guainazzi, M., & Chiaberge, M. 2006, *A&A*, 448, 499
- Boisson, C., & Durret, F. 1986, in *New Insight in Astrophysics, 8 Years of UV Astronomy with IUE (ESA SP-263)*, 687, ed. Rolfe, E.J.
- Brandt, W. N., & Hasinger, G. 2005, *ARA&A*, 43, 827
- Cohen, R.D., Rudy, R.J., Puetter, R.C., Ake, T.B., & Foltz, C.B. 1986, *ApJ*, 311, 135
- Dickey, J. M., & Lockman, F. J. 1990, *ARA&A*, 28, 215
- Dopita, M. A., Pereira, M., Kewley, L. J., & Capaccioli, M. 2002, *ApJS*, 143, 47
- Garcia-Rissmann, A., Vega, L. R., Asari, N. V., Cid Fernandes, R., Schmitt, H., González Delgado, R. M., & Storchi-Bergmann, T. 2005, *MNRAS*, 359, 765
- Georgantopoulos, I., & Zezas, A. 2003, *ApJ*, 594, 704
- Gezari, S., Halpern, J. P., Komossa, S., Grupe, D., & Leighly, K. M. 2003, *ApJ*, 592, 42

- Guainazzi, M., Fiore, F., Matt, G., & Perola, G.C. 2001, MNRAS, 327, 323
- Heckman, T. M., Kauffmann, G., Brinchmann, J., Charlot, S., Tremonti, C., & White, S. D. M. 2004, ApJ, 613, 109
- Heckman, T., et al. 1995, ApJ, 452, 549
- Heckman, T. M., et al. 2005, ApJ, 634, 161
- Hornschemeier, A. E., et al. 2005, AJ, 129, 86
- Huchra, J., & Burg, R. 1992, ApJ, 393, 90
- Kennicutt, R. C. 1998, ApJ, 498, 541
- Khachikian, E.Y., & Weedman, D.W. 1974, ApJ, 192, 581
- Laor, A. 2003, ApJ, 590, 86
- Levenson, N. A., Heckman, T. M., Krolik, J. H., Weaver, K. A., & Życki, P. T. 2006, ApJ, in press (astro-ph/0605438)
- Lumsden, S.L., Alexander, D.M., & Hough, J.H. 2004, MNRAS, 348, 1451
- Lumsden, S.L., Heisler, C.A., Bailey, J.A., Hough, J.H., & Young, S. 2001, MNRAS, 327, 459
- Maiolino, R., Salvati, M., Bassani, L., Dadina, M., della Ceca, R., Matt, G., Risaliti, G., & Zamorani, G. 1998, A&A, 338, 781
- Malkan, M.A., Gorjian, V., & Tam, R. 1998, ApJS, 117, 25
- Moran, E.C., Barth, A.J., Kay, L.E., & Filippenko, A.V. 2000, ApJ, 540, L73
- Mulchaey, J. S., Koratkar, A., Ward, M. J., Wilson, A. S., Whittle, M., Antonucci, R. R. J., Kinney, A. L., & Todd, H. 1994, ApJ, 436, 586
- Murray, N., & Chiang, J. 1998, ApJ, 494, 125
- Nelson, C. H., & Whittle, M. 1995, ApJS, 99, 67
- Nicastro, F. 2000, ApJ, 530, L65
- Nicastro, F., Martocchia, A., & Matt, G. 2003, ApJ, L13
- Osterbrock, D. E., & Martel, A. 1993, ApJ, 414, 552
- Panessa, F., & Bassani, L. 2002, A&A, 394, 435
- Pappa, A., Georgantopoulos, I., Stewart, G. C., & Zezas, A. L. 2001, MNRAS, 326, 995

- Penston, M.V., & Perez, E. 1984, MNRAS, 211, 33
- Pérez García, A. M., & Rodríguez Espinosa, J. M. 2001, ApJ, 557, 39
- Peterson, B.M. 1997, An Introduction to Active Galactic Nuclei, Cambridge Univ. Press
- Peterson, B.M., et al. 2004, ApJ, 613, 682
- Pogge, R.W., & Martini, P. 2002, ApJ, 369, 624
- Pogge, R. W., et al. 2006, in prep.
- Regan, M.W., & Mulchaey, J.S. 1999, AJ, 117, 2676
- Sandage, A., & Tammann, G.A. 1987, A Revised Shapley-Ames Catalog of Bright Galaxies (Publ. 635; Washington D.C.; Carnegie Institute of Washington)
- Tran, H.D. 2001, ApJ, 554, L19
- Whittle, M. 1992, ApJS, 79, 49

Table 1. *Chandra* Observations

Target	z	Coordinates (J2000)		Obs. Date	ObsID	Exp. Time (ks)
		RA	Dec			
IC 3639	0.011	12 40 52.9	−36 45 22.0	2004 Mar 07	4844	8.7
NGC 3982	0.004	11 56 28.1	+55 07 31.0	2004 Jan 03	4845	9.2
NGC 5283	0.010	13 41 05.7	+67 40 20.0	2003 Nov 24	4846	8.9
NGC 5427	0.009	14 03 26.1	−06 01 51.0	2004 Mar 26	4847	8.8

Table 2. X-ray Measurements

Target	Counts		HR ^b
	Broad ^a	Hard ^a Soft ^a	
IC 3639	283.4 ± 16.9	24.8 ± 5.0 258.7 ± 16.2	-0.83 ± 0.03
NGC 3982	73.0 ± 8.7	11.0 ± 3.3 62.1 ± 8.0	-0.70 ± 0.08
NGC 5283	454.4 ± 21.4	337.4 ± 18.4 117.1 ± 10.9	$+0.48 \pm 0.04$
NGC 5427	34.8 ± 6.0	1.8 ± 1.4 33.0 ± 5.8	-0.90 ± 0.08

^aAll counts are net counts after background subtraction. Energy bands are defined as follows: Broad 0.3–8.0 keV, Hard 2.5–8.0 keV, Soft 0.3–2.5 keV.

^bHardness ratio, $HR = (H-S)/(H+S)$, where H and S are the net counts in the hard and soft bands respectively.

Table 3. X-Ray Spectral Fits

Target	Galactic N_{H}^{a}	Model ^b	Spectral Fit Parameters			Fig.	$\chi^2_{\nu}(\text{dof})$
			kT(keV)	N_{H}^{a}	Γ		
IC 3639 all	4.89	ab(br+pl)	0.11 ± 0.03	84 ± 24	2.61 ± 0.60	2	0.91(7)
NGC 3982 all	1.23	ga(pl)	3.7 ± 0.9	4	3.3(2)
NGC 5283 all	1.84	ga(br+ab(pl))	0.71 ± 0.27	730 ± 395	0.76 ± 0.66	6	0.69(16)
extended		ga(br+ab(pl))	0.69 ± 0.33	669 ± 28	-0.13 ± 1.16	7	0.30(5)
core		ga(br+ab(pl))	0.58 ± 0.39	985 ± 8	1.46 ± 0.34	7	0.60(18)
NGC 5427 all	2.38	ga(br)	0.7 ± 0.3	10	0.2(4)

^aColumn density in units of 10^{20} cm^{-2} (Dickey & Lockman 1990).

^bModel labels: **ab**=**xswabs**, photoelectric absorption; **ga**=**xswabs** with value frozen at Galactic column density towards this target; **br**=**xsbremss**, thermal bremsstrahlung; **pl**=**powlaw1d**, one-dimensional power law.

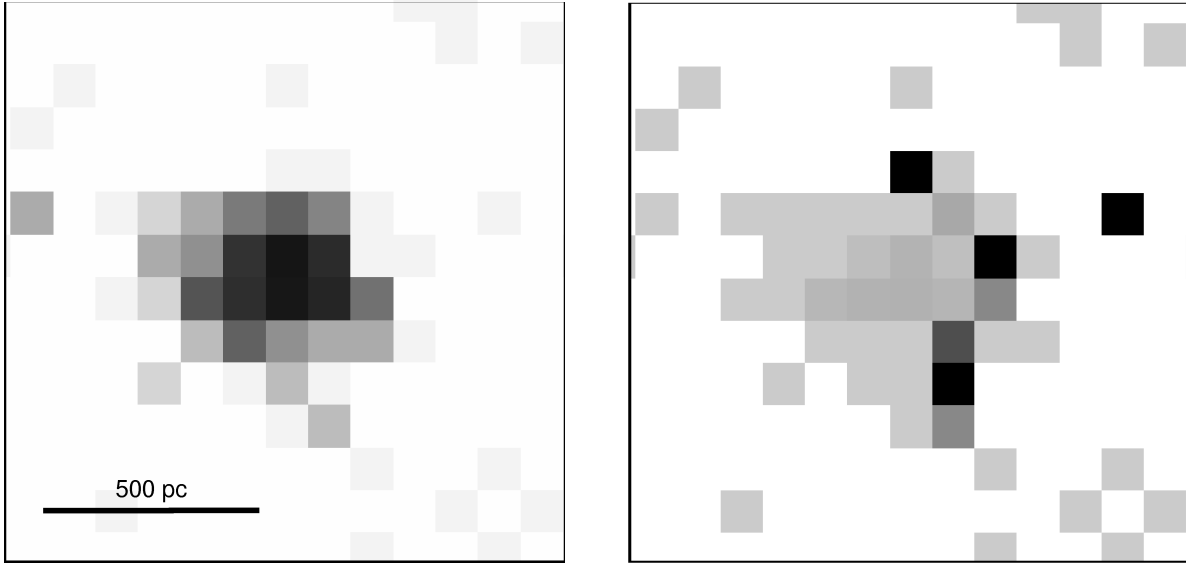


Fig. 1.— *Left:* *Chandra* image of the nucleus of IC 3639 (283 counts detected). There is extended circumnuclear emission in addition to the point source. The solid black bar in the lower left represents a projected distance of 500 pc. *Right:* Hardness ratio (HR; defined in §3) map of the nucleus, showing that most of the emission is in the soft band. Each pixel is colored according to the hardness ratio of the photons in that pixel. The lightest pixels show $HR = -1$, with pixels becoming darker as the HR increases; the darkest pixels have $HR = +1$. Both panels are $6.5''$ on a side. North is up and East is to the left in both panels.

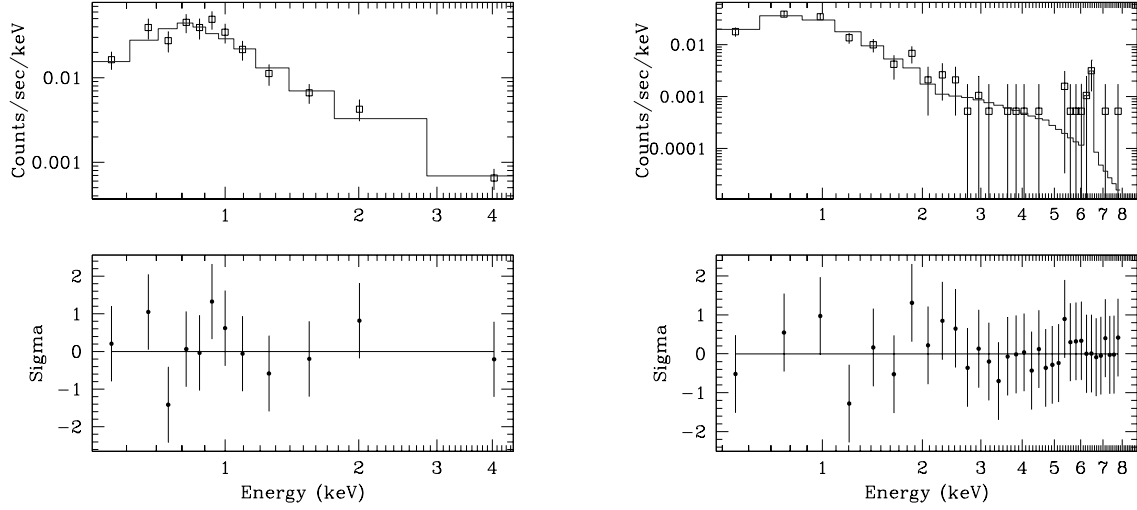


Fig. 2.— Spectrum of IC 3639. The data include both the point source and the extended component. *Left:* Spectrum fit to an absorbed power law plus thermal bremsstrahlung model. In the upper panel, the squares with the error bars are the data and the solid line the best-fit model, which is a power-law with photon index $\Gamma = 2.61 \pm 0.60$ plus thermal bremsstrahlung with a characteristic temperature given by $kT = 0.11 \pm 0.03$ keV, both absorbed by an equivalent hydrogen column density $N_{\text{H}} = (8.9 \pm 2.4) \times 10^{21} \text{ cm}^{-2}$. The lower panel shows the residuals from the fit. *Right:* Spectrum fit to an absorbed bremsstrahlung plus reflected power law model, with an emission line at 6.38 ± 0.06 keV. The best-fit parameters are as follows: $N_{\text{H}} = (4.2 \pm 0.4) \times 10^{21} \text{ cm}^{-2}$, $kT = 0.20 \pm 0.02$ keV, $\Gamma = 2.14 \pm 0.79$. The nominal line equivalent width (~ 500 eV) and the fraction of reflected light in the spectrum ($R \sim 0.6$) are reasonable but totally unconstrained by the fit. The lower panel shows the residuals from the fit.

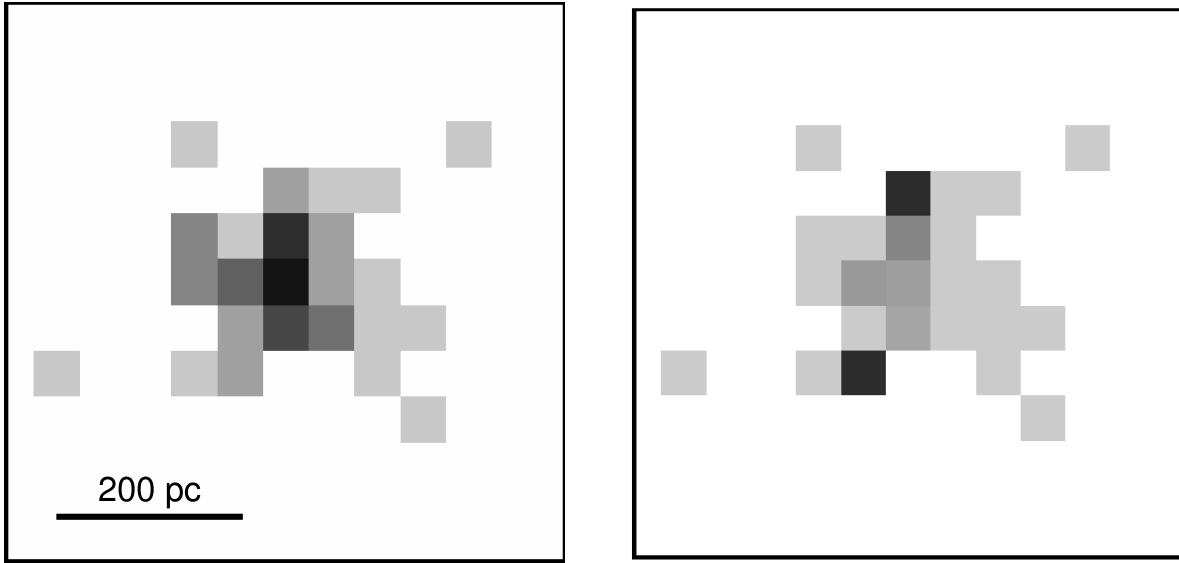


Fig. 3.— *Left*: *Chandra* image of the nucleus of NGC 3982 (73 counts detected). The solid black bar in the lower left represents a projected distance of 200 pc. *Right*: Hardness ratio (HR; defined in §3) map of the nucleus, showing that most of the emission is in the soft band. Each pixel is colored according to the hardness ratio of the photons in that pixel. The lightest pixels show $HR = -1$, with pixels becoming darker as the HR increases; the darkest pixels have $HR = 0$. Both panels are $6''$ on a side. North is up and East is to the left in both panels.

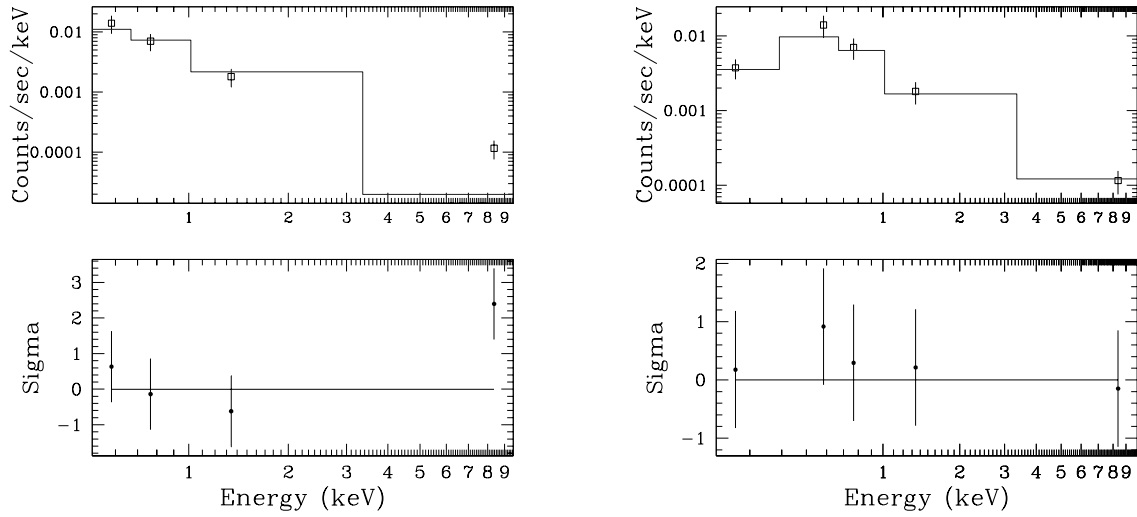


Fig. 4.— Spectrum of NGC 3982 compared to two models. *Left:* The squares show the binned data points and the solid line shows the “best-fit” power law, $\Gamma = 3.7 \pm 0.9$, with only Galactic absorption ($1.23 \times 10^{20} \text{ cm}^{-2}$). The lowest-energy point, seen in the right panel, was not used in estimating the slope of the power law. The lower panel shows the residuals. *Right:* The squares show the binned data points and the solid line shows an absorbed thermal bremsstrahlung plus power law model, where absorption is a free parameter but Γ and kT are kept fixed. The parameter values are $kT = 0.13 \text{ keV}$ and $\Gamma = 1.0$ with $N_H = (2.34 \pm 0.85) \times 10^{21} \text{ cm}^{-2}$. The lower panel shows the residuals.

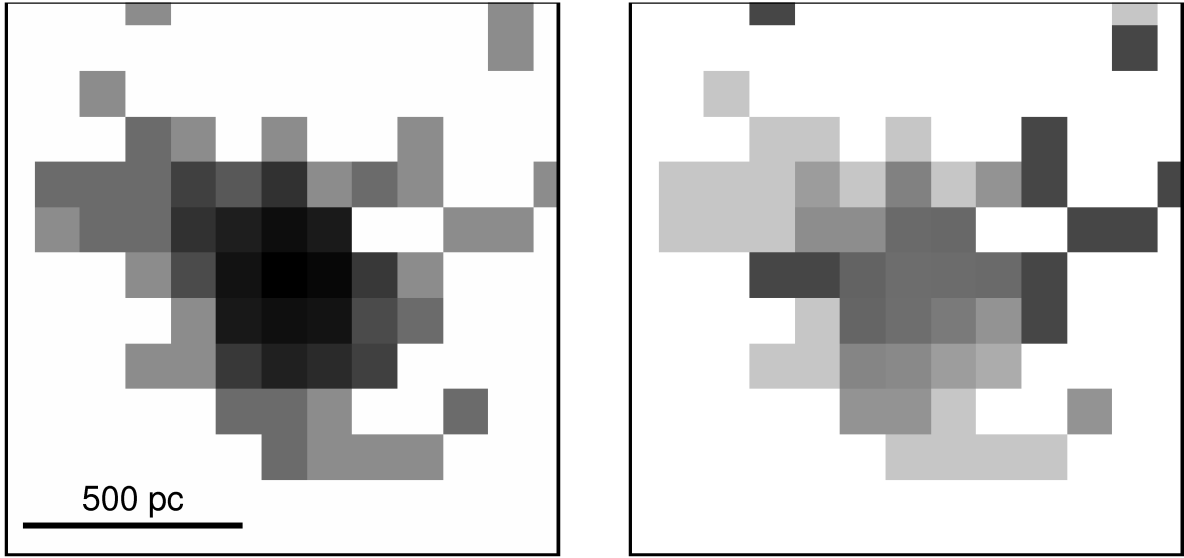


Fig. 5.— *Left:* *Chandra* image of the nucleus of NGC 5283 (454 counts detected). The solid black bar in the lower left represents a projected distance of 500 pc. *Right:* Hardness ratio (HR; defined in §3) map of the nucleus, showing that most of the emission is in the hard band. However, the most extended emission is also the softest. Each pixel is colored according to the hardness ratio of the photons in that pixel. The lightest pixels show $HR = -1$, with pixels becoming darker as the HR increases; the darkest pixels have $HR = +1$. Both panels are $6''$ on a side. North is up and East is to the left in both panels.

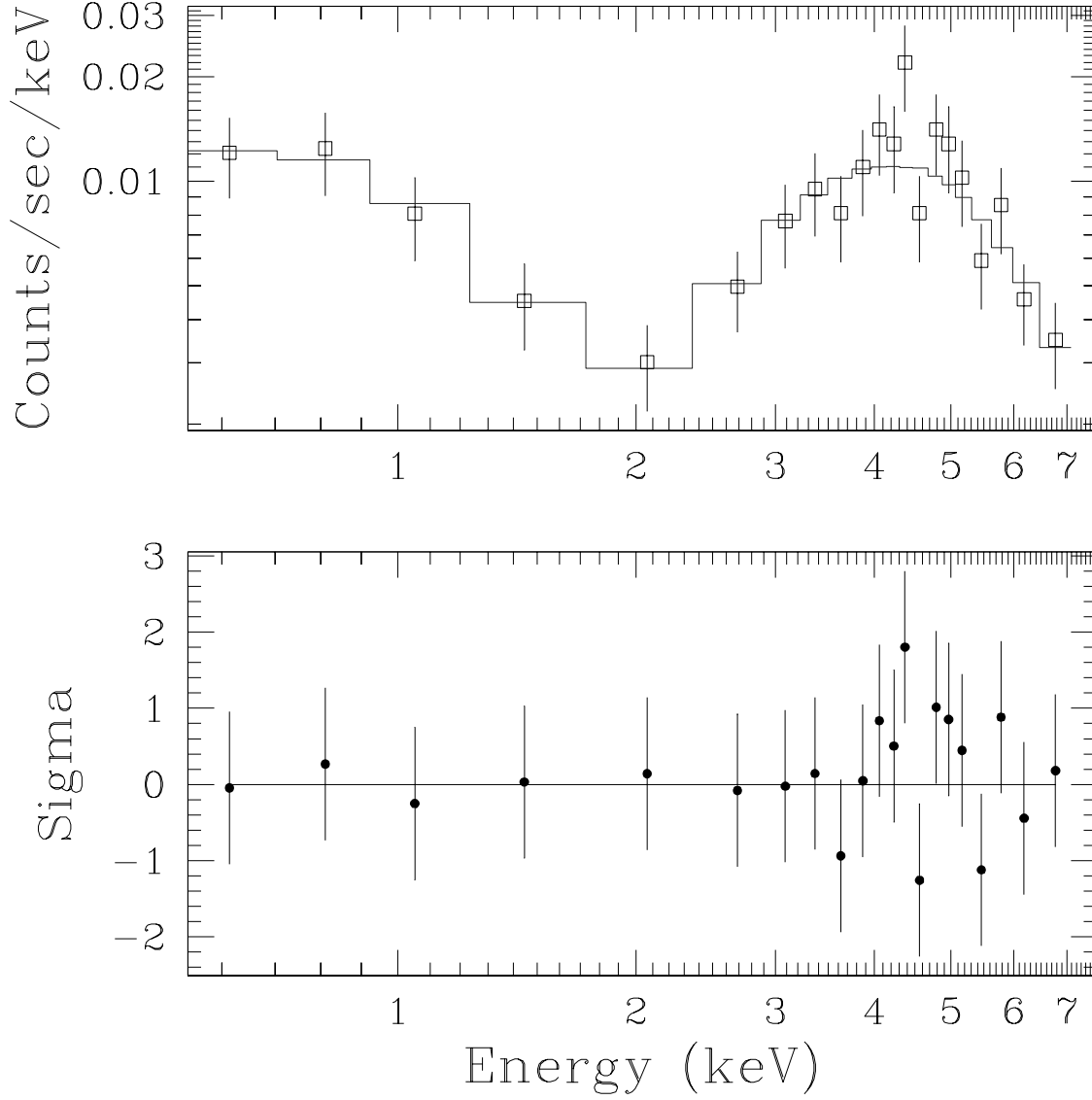


Fig. 6.— Spectrum of NGC 5283 including both the point source and extended emission. The squares show the binned data points and the solid line the best-fit model. The model consists of an absorbed power law ($\Gamma = 0.76 \pm 0.65$, $N_{\text{H}} = [7.3 \pm 3.0] \times 10^{22} \text{ cm}^{-2}$) and thermal emission ($kT = 0.71 \pm 0.27 \text{ keV}$). The Galactic neutral hydrogen column density is $N_{\text{H}} = 1.84 \times 10^{20} \text{ cm}^{-2}$. The lower panel shows the residuals from the fit.

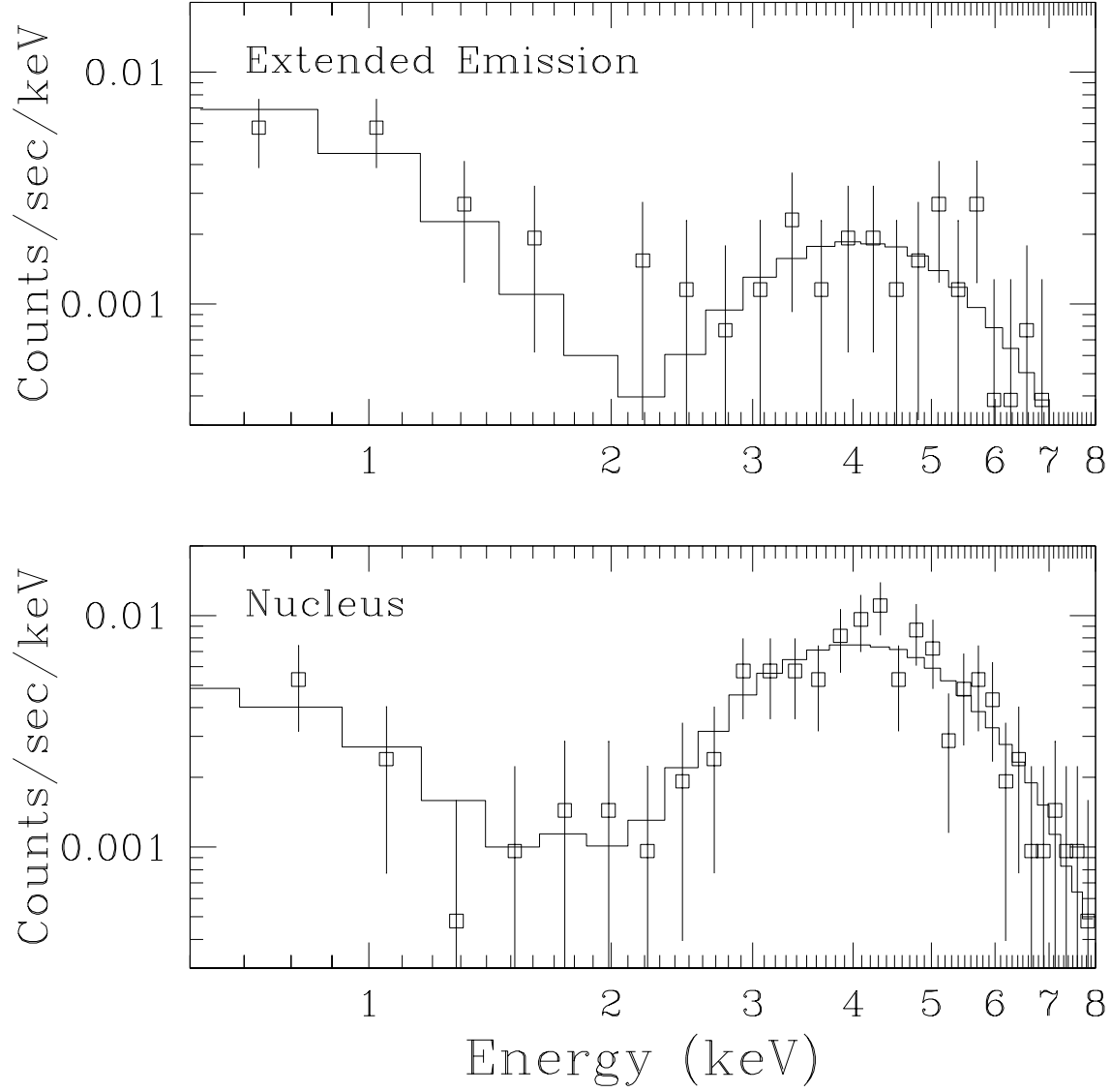


Fig. 7.— Separate spectra of the core and surrounding region of the nucleus of NGC 5283. The top panel shows the spectrum of just the extended emission, with the central 3×3 island masked out. The bottom panel shows the spectrum of just the central pixel. The spectra suggest that the soft, thermal component is emission from the extended emission seen in Fig. 5, while the central source provides the hard, absorbed power law component.

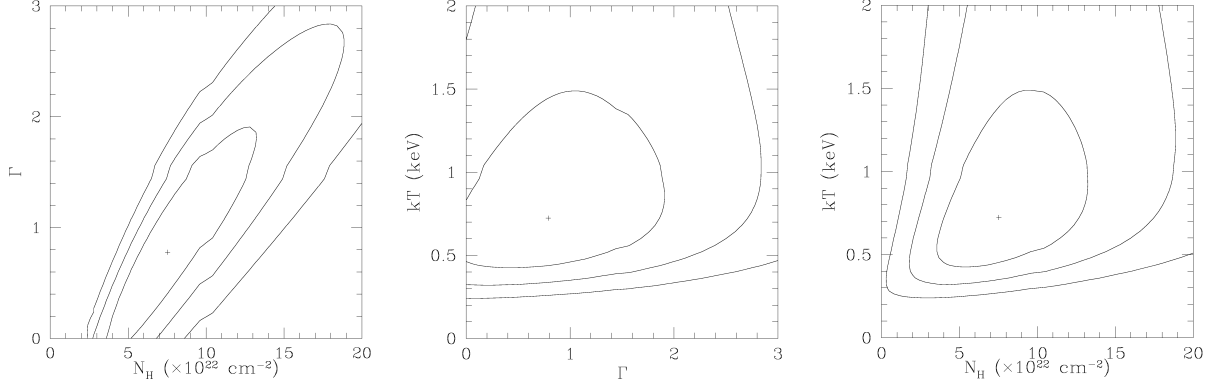


Fig. 8.— Confidence region projections for parameter pairs for the NGC 5283 spectral fit of the point source and extended emission together. A plus sign marks the best-fit value. Contours are drawn at the 1, 2, 3 – σ levels.

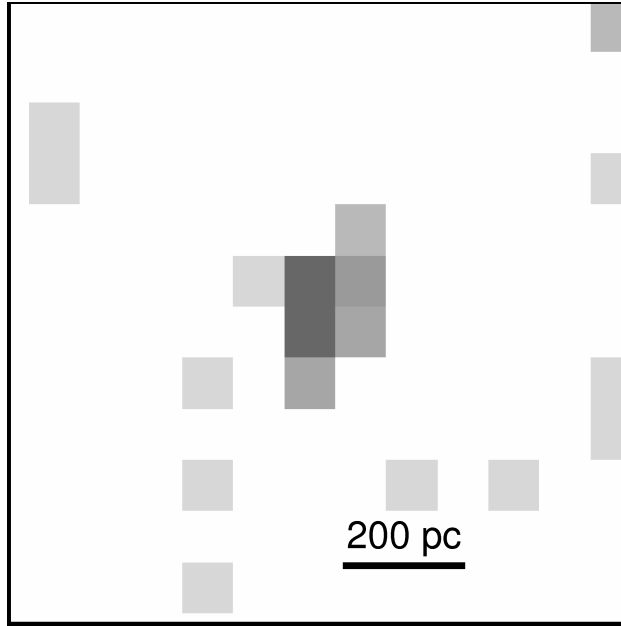


Fig. 9.— *Chandra* image of the nucleus of NGC 5427 (35 counts detected). The solid black line in the lower right represents a projected distance of 200 pc. The image is 6'' on a side. North is up and East is to the left.

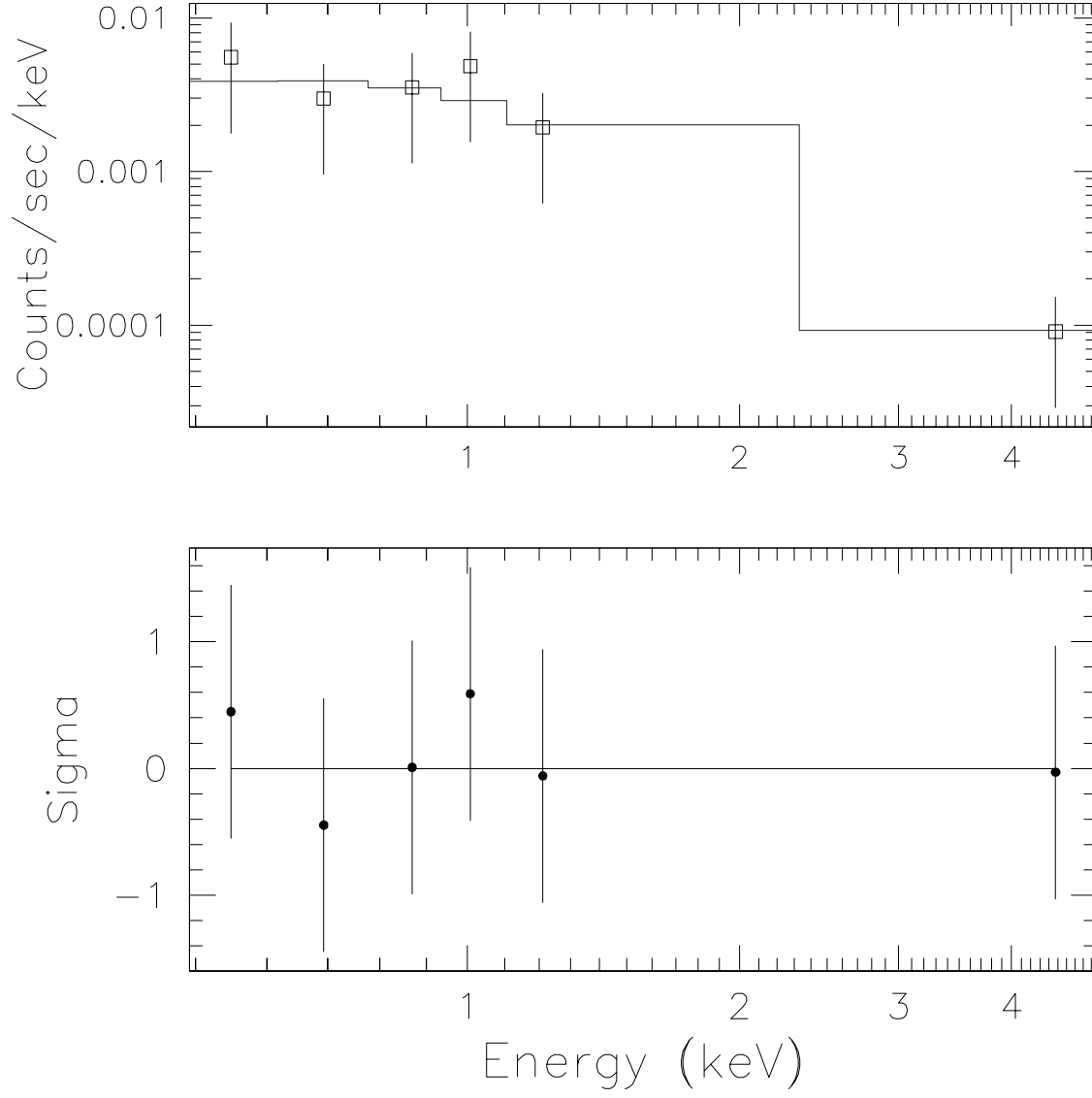


Fig. 10.— Spectrum of NGC 5427, binned so that each bin has at least 5 counts. The solid line shows a thermal bremsstrahlung model characterized by $kT \sim 0.7$ keV with Galactic absorption ($N_H = 2.38 \times 10^{20} \text{ cm}^{-2}$). The lower panel shows the residuals.

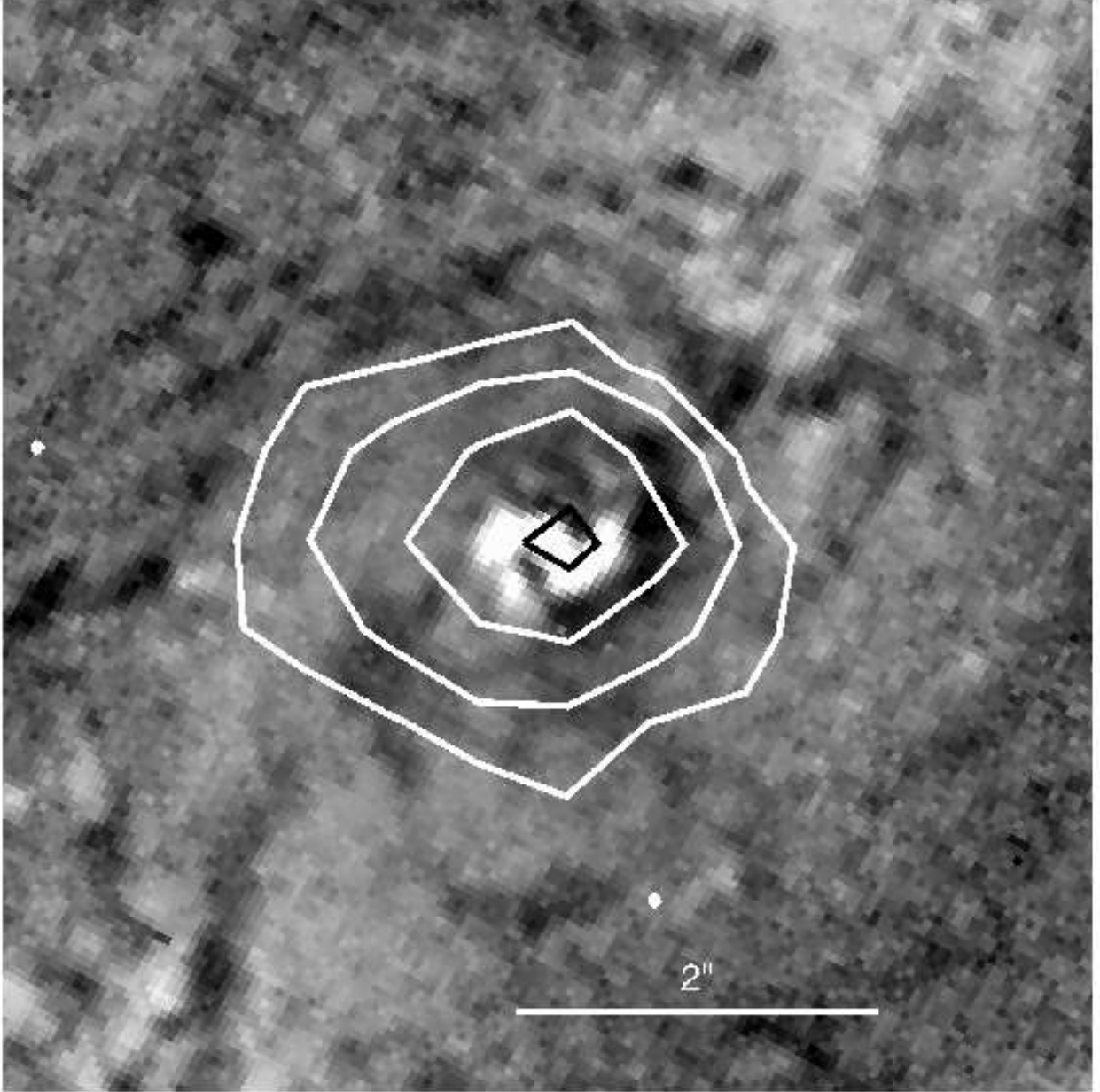


Fig. 11.— Structure map of the nucleus of IC 3639 with X-ray contours overlaid. The structure map is derived from an *HST* image taken using the F606W filter. The bright region near the center is the narrow-line region. The X-ray contours show extension in the East-West direction, as does the NLR. The image is $6''$ on a side, and the white bar on the lower right represents $2''$ (~ 400 pc). The contours are drawn at levels of 2.5, 6.3, 15.8 and 39.8 photons per pixel. The innermost contour is plotted in black to enhance visibility. North is up and East is to the left in the image.

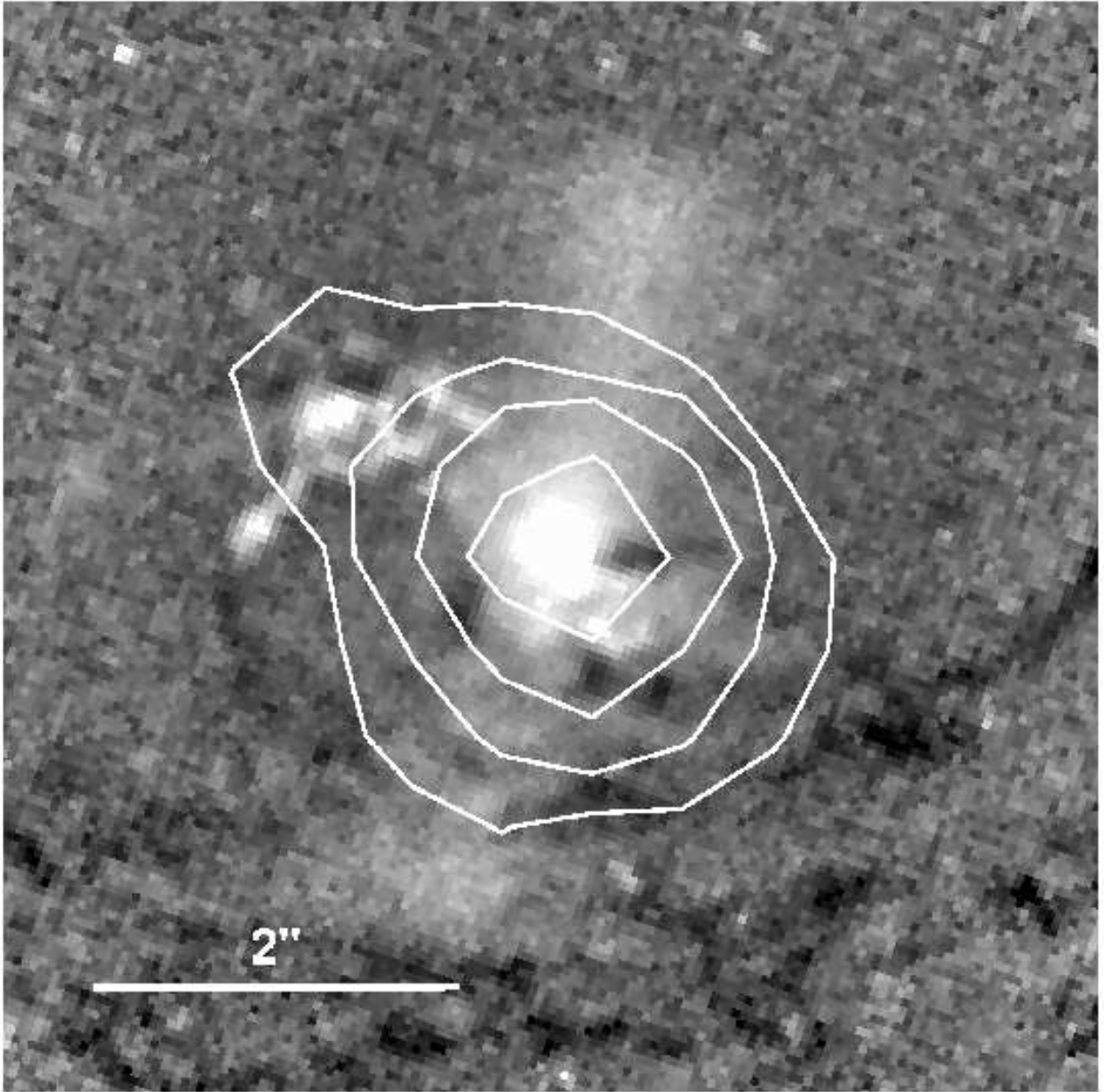


Fig. 12.— Structure map of the nucleus of NGC 5283 with X-ray contours overlaid. The structure map is derived from an *HST* image taken using the F606W filter. North is up and East is to the left in the image. The sharp bright regions near the center show emission from the narrow-line region. The X-ray contours show significant extension in the same direction as the region of enhanced narrow-line emission seen on the structure map. The diffuse bar-like structure running roughly Northwest–Southeast is stellar. The image is 6'' on a side, and the white bar on the lower left represents 2'' (~ 450 pc). The contours are drawn at levels of 2.5, 6.3, 15.8 and 39.8 photons per pixel.